

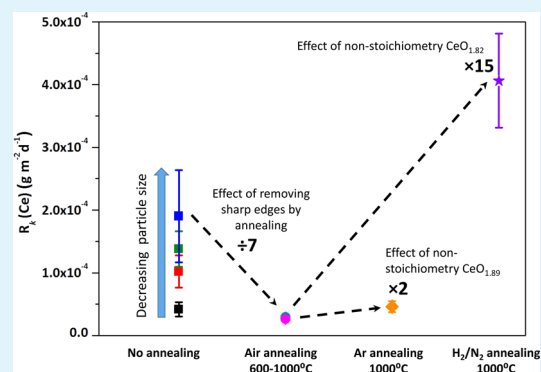
# Role of Microstructure and Surface Defects on the Dissolution Kinetics of CeO<sub>2</sub>, a UO<sub>2</sub> Fuel Analogue

Claire L. Corkhill,\* Daniel J. Bailey, Florent Y. Tocino, Martin C. Stennett, James A. Miller, John L. Provis, Karl P. Travis, and Neil C. Hyatt\*

Immobilisation Science Laboratory, Department of Materials Science and Engineering, The University of Sheffield, Sir Robert Hadfield Building, Mappin Street, Sheffield S1 3JD, U.K.

**ABSTRACT:** The release of radionuclides from spent fuel in a geological disposal facility is controlled by the surface mediated dissolution of UO<sub>2</sub> in groundwater. In this study we investigate the influence of reactive surface sites on the dissolution of a synthesized CeO<sub>2</sub> analogue for UO<sub>2</sub> fuel. Dissolution was performed on the following: CeO<sub>2</sub> annealed at high temperature, which eliminated intrinsic surface defects (point defects and dislocations); CeO<sub>2-x</sub> annealed in inert and reducing atmospheres to induce oxygen vacancy defects and on crushed CeO<sub>2</sub> particles of different size fractions. BET surface area measurements were used as an indicator of reactive surface site concentration. Cerium stoichiometry, determined using X-ray Photoelectron Spectroscopy (XPS) and supported by X-ray Diffraction (XRD) analysis, was used to determine oxygen vacancy concentration. Upon dissolution in nitric acid medium at 90 °C, a quantifiable relationship was established between the concentration of high energy surface sites and CeO<sub>2</sub> dissolution rate; the greater the proportion of intrinsic defects and oxygen vacancies, the higher the dissolution rate. Dissolution of oxygen vacancy-containing CeO<sub>2-x</sub> gave rise to rates that were an order of magnitude greater than for CeO<sub>2</sub> with fewer oxygen vacancies. While enhanced solubility of Ce<sup>3+</sup> influenced the dissolution, it was shown that replacement of vacancy sites by oxygen significantly affected the dissolution mechanism due to changes in the lattice volume and strain upon dissolution and concurrent grain boundary decohesion. These results highlight the significant influence of defect sites and grain boundaries on the dissolution kinetics of UO<sub>2</sub> fuel analogues and reduce uncertainty in the long term performance of spent fuel in geological disposal.

**KEYWORDS:** nuclear fuel, dissolution, defects, oxygen vacancies, grain boundaries



## 1. INTRODUCTION

Spent nuclear fuel is a heterogeneous ceramic material composed primarily of UO<sub>2</sub>, with a minor component of actinides and fission products. The internationally supported strategy for the safe disposal of this nuclear waste material is within a geological disposal facility,<sup>1</sup> where the release of radionuclides to the environment will be dominated by the interaction of the UO<sub>2</sub> matrix with groundwater. To assess the long-term performance of the geological disposal site toward the containment of radionuclides, a safety case is being prepared, which assesses the mechanism and kinetics of fuel dissolution; accordingly, a large number of laboratory experiments have been focused on determining the dissolution kinetics of UO<sub>2</sub> under a wide variety of temperature and redox conditions.<sup>2,3</sup> However, dissolution rates determined from natural uraninite (UO<sub>2</sub>) ore weathering indicate that rates measured in the laboratory are orders of magnitude greater than in nature.<sup>4,5</sup> This phenomenon has been widely considered and is attributed to a number of factors including artifacts of specimen preparation, solution saturation state, and changes in surface area with time.<sup>6</sup> Clearly, it is important to

the development of a robust postclosure safety case for spent fuel disposal that such uncertainty is reduced.

In the current study, we consider the role of “energetically reactive sites”, which contain fewer, and weaker, chemical bonds than those on defect-free surfaces or in the bulk, in the determination of laboratory dissolution rates of spent UO<sub>2</sub> fuel. These sites, which may include natural crystal defects (point defects and dislocations), grain boundaries, or sample preparation-induced artifacts (e.g., polishing scratches or sharp edges on crushed particles), comprise atoms that have greater reactivity than those in the defect-free surfaces or in the bulk, thus may dissolve more rapidly.<sup>7,8</sup> For example, the dissolution of UO<sub>2</sub> and a CeO<sub>2</sub> analogue for UO<sub>2</sub> have been found to be influenced by sample crushing<sup>9,10</sup> and polishing;<sup>11</sup> dissolution rates were overestimated by 3 orders of magnitude due to the reactive surface sites induced through these sample preparation techniques.<sup>11</sup> Natural defects, especially randomly distributed oxygen vacancy defects, dominate the lattice

Received: November 23, 2015

Accepted: March 29, 2016

Published: March 29, 2016

structure of spent  $\text{UO}_2$  fuel, due to the incorporation of trivalent rare earth fission products in the  $\text{UO}_2$  lattice.<sup>12</sup> It has been hypothesized that the presence of such energetically reactive defect sites may influence the dissolution rate.<sup>13–18</sup> However, the extent of such an effect on the overall dissolution rate is difficult to observe when other factors, such as the enhanced solubility of  $\text{U(VI)}$  over  $\text{U(IV)}$ , strongly influence the dissolution behavior. Recent work by the current authors has shown that these seemingly minor features may significantly influence the *initial* dissolution rate of  $\text{UO}_2$  fuel analogues<sup>11,19</sup> and, therefore, should be taken into consideration alongside other important factors (notably oxidation, solubility, and radiolysis) when understanding dissolution mechanisms of spent fuel.

In an attempt to preclude the dominant effects of  $\text{U(IV)}$  oxidation, the high solubility of  $\text{U(VI)}$  and radiolysis on the dissolution kinetics, we here report the role of energetically reactive features on the dissolution of a  $\text{UO}_2$  analogue,  $\text{CeO}_2$ , that was developed to closely resemble the microstructure of  $\text{UO}_2$  fuel.<sup>20</sup> Both  $\text{UO}_2$  and  $\text{CeO}_2$  crystallize in the same fluorite-type structure ( $Fm\bar{3}m$ ) and can be engineered to have similar grain sizes and crystallographically randomly orientated grains. We describe an evaluation of how energetically reactive sites, including intrinsic surface defects and oxygen vacancies, influence dissolution kinetics. Through quantification of these effects, we attempt to improve our understanding of the uncertainties associated with dissolution rates of spent fuel in geological disposal conditions.

## 2. EXPERIMENTAL METHODS

**2.1.  $\text{CeO}_2$  Preparation.** Cerium dioxide monoliths were prepared according to Stennett et al.,<sup>20</sup> at a sintering temperature of 1700 °C. Monoliths were crushed using a percussion mortar and ball mill, sieved to four different size fractions, 25–50  $\mu\text{m}$ , 75–150  $\mu\text{m}$ , 300–600  $\mu\text{m}$ , and 2–4 mm, and washed, all according to ASTM C1285 (the Product Consistency Test).<sup>21</sup> Prior to use, the particles were inspected by Scanning Electron Microscopy (SEM) to ensure no fine particles <1  $\mu\text{m}$  in size remained adhered to particle surfaces. Particles in the size fraction 25–50  $\mu\text{m}$  were subjected to further heat treatment; annealing in air was performed in a standard muffle furnace heated to 300, 400, 600, 800, 1000, and 1250 °C at a ramp rate of 5 °C  $\text{min}^{-1}$  and held for 4 h. Annealing in inert (Ar) and reducing (5%  $\text{H}_2$ /95%  $\text{N}_2$ ) atmospheres was performed in a standard tube furnace, sealed, and purged with gas for 2 h prior to heating to 1000 °C at a ramp rate of 5 °C  $\text{min}^{-1}$  and held for 4 h. Following dissolution, particles were dried by patting with tissue and placed in an inert-atmosphere desiccator prior to analysis.

**2.2. Particle Characterization.** The surface area of each crushed size fraction and the 25–50  $\mu\text{m}$  heat-treated particles was determined using the Brunauer, Emmett, and Teller (BET) method, using a nitrogen adsorbate. Particles were degassed for 3 h at 200 °C and analyzed using a Beckman Coulter SA3100 instrument. The surface oxidation state of annealed particles was determined using a Kratos Axis Ultra X-ray Photoelectron Spectrometer (XPS) with a monochromatic Al  $K\alpha$  source. The spectral intensities recorded were converted to surface oxidation state concentrations by first subtracting a Shirley-type background<sup>22</sup> and then obtaining accurate peak positions by fitting peaks using a mixed Gaussian/Lorentzian line shape. All photoelectron binding energies were referenced to C 1s adventitious contamination peaks at a binding energy of 285 eV.

Powder X-ray Diffraction (XRD) patterns were acquired using a Bruker D2 Phaser diffractometer operating in reflection mode at 30 kV and 10 mA with Cu  $K\alpha_1$  radiation. Data were collected between  $20 < 2\theta < 60^\circ$  at  $2^\circ \text{min}^{-1}$  and a step size of  $0.02^\circ$ . Rietveld analysis of phases identified in the diffraction patterns was performed using the refinement software, Topas (Bruker), and strain was calculated using

the Double-Voigt approach.<sup>23</sup> Secondary electron images of particles were acquired using a Hitachi TM3030 SEM, operating at an accelerating voltage of 15 kV and a working distance of 18 mm.

**2.3.  $\text{CeO}_2$  Dissolution.** Samples of 0.1 g of each size fraction of  $\text{CeO}_2$  particles were placed in 50 mL PTFE vessels, which had been cleaned according to ASTM C1285.<sup>21</sup> Each vessel was filled with 40 mL of 0.01 M  $\text{HNO}_3$  (pH 2.0), sealed, and placed within a Carbolite oven. For 25–50  $\mu\text{m}$   $\text{CeO}_2$  particles with no annealing treatment, experiments were performed at 40, 70, and 90 °C ( $\pm 0.5^\circ\text{C}$ ). All other experiments were performed at 90 ( $\pm 0.5$ ) °C. Each experiment was performed in triplicate with duplicate blanks, and sampling was conducted at regular intervals from 0 to 35 days. During each sampling, an aliquot (1.2 mL) of the supernatant liquid in each vessel was removed and filtered (0.22  $\mu\text{m}$ ) prior to analysis by Inductively Coupled Plasma – Mass Spectroscopy (ICP-MS) (Agilent 4500 Spectrometer). Solution data expressed as the normalized weight loss ( $N_L$ , expressed in  $\text{g m}^{-2}$ ) were calculated from the Ce concentrations after normalization by the surface area  $S$  ( $\text{m}^2$ ) of the sample in contact with the solution (assuming that all the surface is “reactive”) and by the mass loading of the element considered in the solid (i.e.,  $f_i$  is expressed as the ratio between the mass of the considered element and the overall mass of the leached sample), according to eq 1<sup>24,25</sup>

$$N_L(i) = \frac{m_i}{f_i \times S} \quad (1)$$

where  $m_i$  (g) corresponds to the total amount of the element  $i$  measured in the solution.

Derivation of eq 1 as a function of dissolution time gives the normalized dissolution rate of Ce ( $R_L(\text{Ce})$ ), expressed in  $\text{g m}^{-2} \text{d}^{-1}$ <sup>26</sup>

$$\begin{aligned} R_L(\text{Ce}) &= \frac{dN_L(\text{Ce})}{dt} = \frac{1}{f_{\text{Ce}} \times S} \times \frac{dm_{\text{Ce}}}{dt} \\ &= \frac{1}{f_{\text{Ce}} \times S} \times \frac{d}{dt}(C_{\text{Ce}} \times V) \approx \frac{V}{f_{\text{Ce}} \times S} \times \frac{dC_{\text{Ce}}}{dt} \end{aligned} \quad (2)$$

where  $C_{\text{Ce}}$  ( $\text{g L}^{-1}$ ) is the concentration of Ce in solution, and  $V$  (L) is volume of leachate. In this expression, the  $f_{\text{Ce}}$  and  $S$  values are usually assumed to remain almost constant during the leaching experiments, which can be considered as a valid assumption at the beginning of the dissolution tests for powdered samples.

## 3. RESULTS

**3.1. Characterization of Defect Structures in  $\text{CeO}_2$ .** Particles from the 25–50  $\mu\text{m}$  size fraction were annealed in air at temperatures ranging from 300–1250 °C. One sample was analyzed without annealing for comparison. High temperature annealing in air lead to a reduction in surface area, as shown in Figure 1. For example, annealing at 600 °C gave a surface area of  $0.20 \pm 0.01 \text{ m}^2 \text{ g}^{-1}$ , while at 1000 °C the surface area was  $0.11 \pm 0.01 \text{ m}^2 \text{ g}^{-1}$ . We hypothesize that the surface area decrease reflects the removal of “sharp edges” and other intrinsic surface defects in the  $\text{CeO}_2$  particles, during heating. When the annealing temperature was increased to the range 700 to 1250 °C, a sharp drop in surface area was observed. This may be due to agglomeration of particles at these higher temperatures. Dissolution rate investigation was performed on samples annealed at 600 and 1000 °C; both were representative of the removal of “sharp edges” and intrinsic surface defects, but samples annealed at 1000 °C additionally represented particles with a significantly lower surface area.

An attempt to generate oxygen vacancies in particles of  $\text{CeO}_2$  in the 25–50  $\mu\text{m}$  size fraction was made by annealing at 1000 °C in the absence of oxygen (inert or reducing environments). The creation of an oxygen vacancy in  $\text{CeO}_2$  is accompanied by the release of two electrons from lattice  $\text{O}^{2-}$ , resulting in the reduction of  $\text{Ce}^{4+}$  ions to  $\text{Ce}^{3+}$ .<sup>27</sup> Reduction from  $\text{CeO}_2$  to

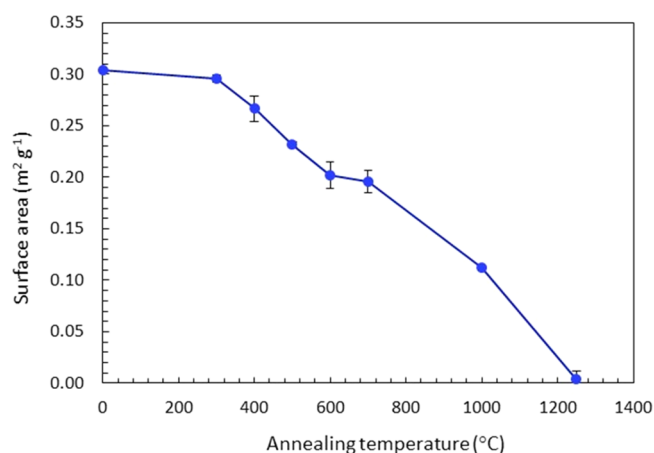


**Figure 1.** Surface area analysis of CeO<sub>2</sub> 25–50 μm particles as a function of annealing temperature, as determined by the BET method. Errors represent 1σ from triplicate samples.

Ce<sub>2</sub>O<sub>3</sub> occurs through the formation of CeO<sub>2-x</sub> intermediate phases;<sup>28</sup> to confirm the presence of oxygen vacancies, the oxidation state of Ce was determined using XPS, shown in Figure 2. Trivalent Ce was identified in the particle surfaces (top ~10 nm), confirming that Ce<sup>4+</sup> reduction to Ce<sup>3+</sup> had

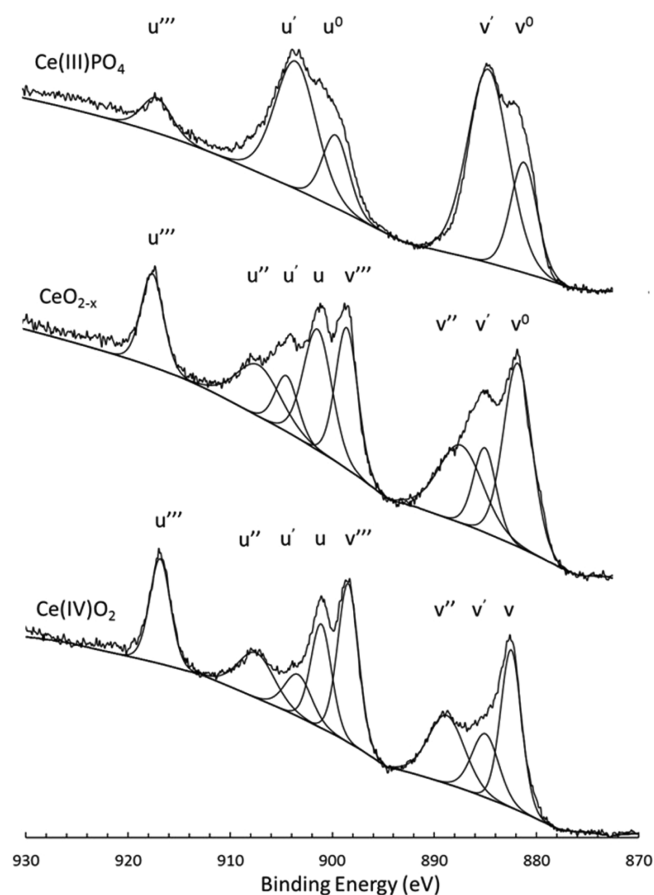


**Figure 2.** X-ray photoelectron oxidation state analysis of CeO<sub>2</sub> annealed under reducing conditions, showing Ce 3d spectra for CeO<sub>2-x</sub> annealed in a reducing (H<sub>2</sub>/N<sub>2</sub>) atmosphere. Standard spectra for Ce<sup>3+</sup>- and Ce<sup>4+</sup>-containing materials are shown for comparison. Peak deconvolution was performed and labeled according to the accepted Burroughs nomenclature<sup>30</sup> for Ce 3d as described in Table 1.

**Table 1.** Experimental Binding Energies and FWHM for Ce 3d Peaks Derived from a CePO<sub>4</sub> Standard and CeO<sub>2</sub> and CeO<sub>2-x</sub> Particles Investigated in the Current Study

Ce 3d peak assignment	oxidation state assignment	binding energy (eV) (±0.1)	fwfm (eV) (±0.05)
v <sup>0</sup>	3+	881.90	3.0
V	3+	882.40	1.8
v'	4+	885.30	4.3
v''	4+	888.40	4.2
v'''	4+	898.50	2.3
u <sup>0</sup>	3+	899.95	3.0
U	3+	901.10	1.8
u'	4+	903.00	4.3
u''	4+	907.60	4.2
u'''	4+	916.80	2.3

occurred. The Ce 3d XPS data were resolved using ten components;<sup>29</sup> Table 1 describes each of the components found in the current study according to the accepted Burroughs nomenclature.<sup>30</sup> These data are in excellent agreement with previously published XPS data for partially reduced CeO<sub>2</sub><sup>31,32</sup> and show that samples annealed in an inert or reducing environment were not fully reduced to Ce<sub>2</sub>O<sub>3</sub> but contained a combination of identifiable contributions from both Ce<sup>3+</sup> and Ce<sup>4+</sup> oxidation states at the sample surface. This indicates the formation of partially reduced CeO<sub>2</sub> with a stoichiometry of CeO<sub>2-x</sub> and the generation of oxygen vacancies. These defects have been previously characterized as Frenkel-type defects.<sup>33</sup>

The fraction of Ce<sup>3+</sup> (denoted α) was determined from Ce 3d peak area analysis, according to eq 3. On the basis that half an oxygen vacancy is formed per Ce<sup>3+</sup> created, the deviation, x, from the ideal oxygen stoichiometry was determined for each sample, as shown in Table 2

$$\alpha = \frac{\text{Ce}^{3+}}{\sum \text{Ce}} \quad (3)$$

**Table 2.** Calculated Surface Stoichiometry and Ce<sup>3+</sup> Fraction (α) of Samples and Standards Investigated in This Study, as Determined from Ce 3d XPS Data<sup>a</sup>

sample treatment	surface stoichiometry	α
Ce(III)PO <sub>4</sub> standard		0.952 ± 0.051
H <sub>2</sub> /N <sub>2</sub> atmosphere 1000 °C	CeO <sub>1.82</sub>	0.370 ± 0.019
Ar atmosphere 1000 °C	CeO <sub>1.89</sub>	0.221 ± 0.011
air 1000 °C	CeO <sub>1.96</sub>	0.080 ± 0.004
air 600 °C	CeO <sub>1.93</sub>	0.143 ± 0.007
air - no annealing	CeO <sub>1.99</sub>	0.021 ± 0.008

<sup>a</sup>Errors quoted for α are standard deviations based upon duplicate XPS scans on each sample.

Annealing in a reducing (H<sub>2</sub>/N<sub>2</sub>) atmosphere resulted in CeO<sub>2-x</sub> with the greatest Ce<sup>3+</sup> fraction (α = 0.370 ± 0.019) and a stoichiometry of CeO<sub>1.82</sub>, while annealing in an inert (Ar) atmosphere gave a higher Ce<sup>3+</sup> fraction than annealing in air under the same conditions (α = 0.221 ± 0.011 and α = 0.080 ± 0.004, respectively). As the Ce<sup>3+</sup> fraction is directly related to the concentration of oxygen vacancies generated, it can be assumed that the oxygen vacancy concentration is proportional to the Ce<sup>3+</sup> fraction of each sample.

The crystal structure of nonstoichiometric CeO<sub>2-x</sub> was determined using X-ray diffraction. Because the samples were



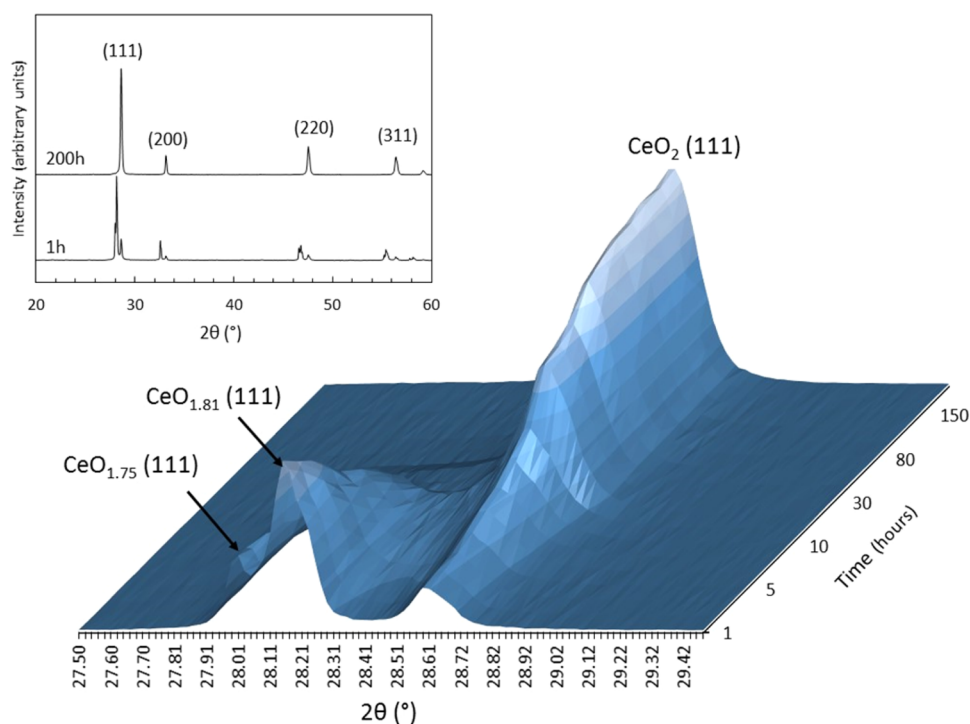


**Figure 3.** X-ray diffraction data for  $\text{CeO}_{2-x}$  formed by annealing  $\text{CeO}_2$  at  $1000\text{ }^\circ\text{C}$  under a reducing atmosphere ( $\text{H}_2/\text{N}_2$ ). XRD patterns were recorded, in air, at regular periods from 0.76 to 200 h after annealing. Correlation of the fluorite lattice parameter with the known oxygen stoichiometry in the  $\text{CeO}_{2-x}$  system<sup>31</sup> allowed diffraction peaks to be identified as  $\text{CeO}_{1.75}$ ,  $\text{CeO}_{1.81}$ , and  $\text{CeO}_2$ . Inset shows full diffraction patterns recorded at 1 h and 200 h, indexing peaks for  $\text{CeO}_2$ .

found to be chemically unstable upon exposure to air, they were loaded into the diffractometer within minutes of being removed from the annealing furnace. By comparison to the known correlation of the fluorite lattice parameter with the oxygen stoichiometry in the  $\text{CeO}_{2-x}$  system,<sup>34</sup> the three main diffraction peaks identified in Figure 3 were assigned to  $\text{CeO}_{1.75}$ ,  $\text{CeO}_{1.81}$ , and  $\text{CeO}_2$ . The second phase is in reasonable agreement with the XPS analysis of this sample, which gave a stoichiometry of  $\text{CeO}_{1.82}$  (Table 2). The  $\text{CeO}_{1.75}$  phase was not identified by XPS; this may be due to the rapid oxidation, as described below. The spatial distribution of the phases within the samples was not investigated, however, since  $\text{Ce}^{3+}$  species have previously been found to accumulate at grain boundaries within partially reduced  $\text{CeO}_2$ ,<sup>35</sup> grain boundaries may host  $\text{CeO}_{1.75}$  and  $\text{CeO}_{1.81}$ . The identification of these phases following annealing in a reducing atmosphere is consistent with the formation of oxygen vacancies.<sup>34</sup>

With prolonged exposure to ambient conditions (air, for up to 200 h), the relative intensity of the peaks assigned to  $\text{CeO}_{1.75}$ ,  $\text{CeO}_{1.81}$ , and  $\text{CeO}_2$  changed (Figure 3). Quantitative Rietveld analysis of the distribution of phases as a function of time is shown in Figure 4. Initially, the sample was composed of  $\sim 15\%$   $\text{CeO}_{1.75}$ ,  $\sim 68\%$   $\text{CeO}_{1.81}$  and  $\sim 16\%$   $\text{CeO}_2$  ( $\pm 1.0\%$ ). After 56 h,  $\text{CeO}_{1.75}$  was no longer observed, and the distribution of phases remained at  $4.5 \pm 0.9\%$   $\text{CeO}_{1.81}$  and  $95.2 \pm 1.3\%$   $\text{CeO}_2$  (Figure 4) until 200 h. The increase in the content of oxygen, corresponding to a decrease in oxygen vacancies, was found to occur at a rate of  $(1.40 \pm 0.14) \times 10^{-3} \text{ mol h}^{-1}$  during the first 24 h of exposure to ambient conditions. This process was associated with a change in the volume of the fluorite unit cell, as calculated from Rietveld-refined lattice parameters. The fluorite unit cell was found to contract, from  $167.62 \pm 3.4 \text{ \AA}^3$  for  $\text{CeO}_{1.75}$  to  $164.97 \pm 3.30 \text{ \AA}^3$  for  $\text{CeO}_{1.81}$  and to  $157.58 \pm$

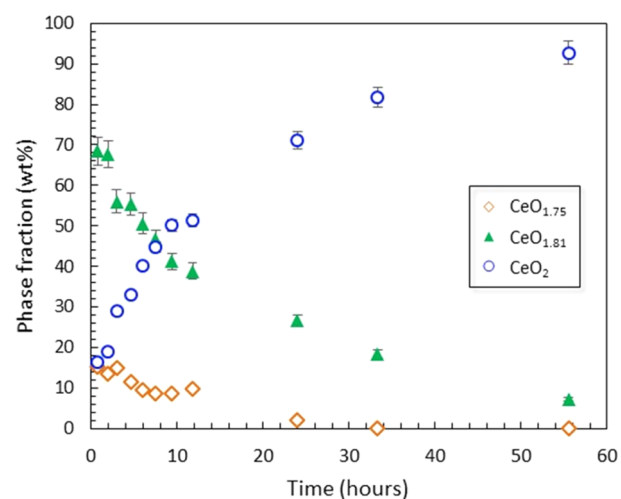


**Figure 4.** Weight fraction of  $\text{CeO}_2$  and  $\text{CeO}_{2-x}$  phases present in a sample of  $\text{CeO}_2$  annealed at  $1000\text{ }^\circ\text{C}$  in a  $\text{H}_2/\text{N}_2$  atmosphere as a function of time, as determined by quantitative Rietveld analysis of powder XRD patterns. After 56 h, there was no further change in the distribution of phases up to 200 h of observation. Errors are  $\pm 3\%$  based on Rietveld analysis methods.

$3.15 \text{ \AA}^3$  for  $\text{CeO}_2$ . This volume reduction is consistent with the oxidation of  $\text{Ce}^{3+}$  to  $\text{Ce}^{4+}$ ;  $\text{Ce}^{3+}$  has a larger ionic radius than  $\text{Ce}^{4+}$  (1.03 and 0.97  $\text{ \AA}$ , respectively).<sup>36</sup> Overall, the sample annealed in a  $\text{H}_2/\text{N}_2$  atmosphere underwent a 6% volume contraction within several hours of exposure to oxygen under ambient atmospheric conditions. The lattice strain, as calculated using Rietveld analysis of the  $\text{CeO}_2$  phase, was found to significantly decrease during oxidation, from a value of  $\varepsilon = 0.092 \pm 0.01$  at 2 h to  $\varepsilon = 0.034 \pm 0.01$  after 200 h, consistent

with the observed change in lattice volume. Due to the rapid nature of these chemical and structural changes, all dissolution experiments were performed within 30 min of sample annealing to minimize the effects of air oxidation.

**3.2. CeO<sub>2</sub> Dissolution.** Cerium dioxide dissolution experiments were performed under aggressive conditions (0.01 M HNO<sub>3</sub>, 90 °C) to attain quantitative dissolution kinetic data within several weeks. It has been suggested that reduction of Ce<sup>4+</sup> to Ce<sup>3+</sup> may be induced by nitrous acid (HNO<sub>2</sub>) formed through nitric acid instability at high acidity (>0.5 M);<sup>13</sup> however, this is not expected to influence the dissolution reaction in the current experiments, which were at an acidity much less than 0.5 M.

The dissolution of CeO<sub>2</sub> can be described by two distinct regimes, as shown in Figure 5; the first, rapid regime is far from

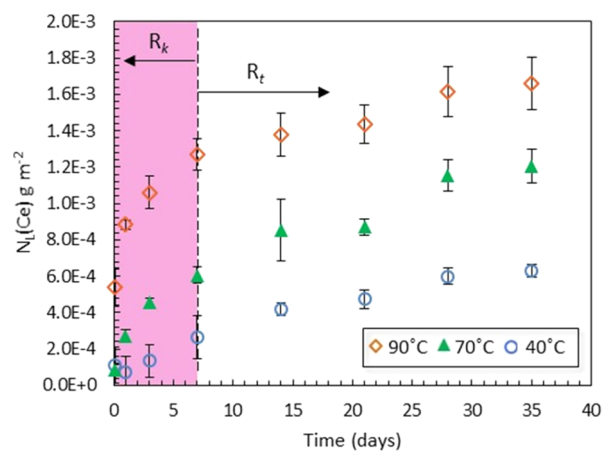


**Figure 5.** Concentration of Ce, normalized to surface area ( $\text{g m}^{-2}$ ) for non-annealed CeO<sub>2</sub> particles 25–50  $\mu\text{m}$  in size, reacted in 0.01 M HNO<sub>3</sub> at 40, 70, and 90 °C, as a function of time. Graph depicts the two main dissolution rates observed, kinetically controlled dissolution ( $R_k$ ) and thermodynamic effect-controlled dissolution ( $R_t$ ). Errors represent  $1\sigma$  from triplicate samples.

solution saturation and thus represents the kinetically controlled dissolution rate,  $R_k$ . The second regime is representative of near-solution saturation, controlled by the solubility of CeO<sub>2</sub> and concentration of Ce(OH)<sub>2</sub><sup>2+</sup> in solution. This is less rapid due to thermodynamic effects that occur close to equilibrium and is denoted  $R_t$ . To understand the role of defects in the dissolution of CeO<sub>2</sub>, it was necessary to focus only on the kinetic regime of dissolution; therefore, we herein report  $R_k$  only. Generally, the change between the kinetic and the thermodynamically controlled dissolution regimes occurred at  $\sim 7$  days, unless otherwise stated. Figure 5 shows the normalized mass loss of Ce ( $N_L$ ,  $\text{g m}^{-2}$ ) from nonannealed 25–50  $\mu\text{m}$  particles of CeO<sub>2</sub> as a function of time at 40, 70, and 90 °C. The normalized dissolution rate of Ce was  $R_k = (1.90 \pm 0.74) \times 10^{-4} \text{ g m}^{-2} \text{ d}^{-1}$  at 90 °C. The dependence of dissolution on temperature gave an activation energy of  $30.4 \pm 4 \text{ kJ mol}^{-1}$ , assuming an Arrhenius-type relationship. This is consistent with previous work on CeO<sub>2</sub> and other fluorite-type dioxides such as ThO<sub>2</sub> and PuO<sub>2</sub> ( $E_a = 20\text{--}37 \text{ kJ mol}^{-1}$ )<sup>13,25,37</sup> and is indicative of a surface-controlled dissolution mechanism.

**3.3. Effect of Defect Annealing/Surface Area on CeO<sub>2</sub> Dissolution Kinetics.** The dissolution rates of 25–50  $\mu\text{m}$  particles of CeO<sub>2</sub> annealed in air, and nonannealed CeO<sub>2</sub> of four different particle sizes, are shown in Table 3 and Figure 6.

**Table 3.** Calculated Dissolution Rates ( $R_k$ ) for CeO<sub>2</sub> and CeO<sub>2-x</sub> Reacted in 0.01 M HNO<sub>3</sub> at 90 °C between 0 and 35 Days of Dissolution, with the Corresponding Measured Surface Area and Oxygen Vacancy Content (Ce<sup>3+</sup> Fraction,  $\alpha$ )

sample treatment	surface area ( $\text{m}^2 \text{ g}^{-1}$ )	$\alpha$	$R_k$ ( $\text{g m}^{-2} \text{ d}^{-1}$ )
<i>25–50 <math>\mu\text{m}</math> samples</i>			
H <sub>2</sub> /N <sub>2</sub> atmosphere 1000 °C <sup>a</sup>	0.53 $\pm$ 0.01	0.370 $\pm$ 0.019	
H <sub>2</sub> /N <sub>2</sub> atmosphere 1000 °C <sup>b</sup>	2.49 $\pm$ 0.02	0.090 $\pm$ 0.003	(4.06 $\pm$ 0.75) $\times 10^{-4}$
Ar atmosphere 1000 °C	0.20 $\pm$ 0.01	0.221 $\pm$ 0.011	(4.62 $\pm$ 0.90) $\times 10^{-5}$
Air 1000 °C	0.11 $\pm$ 0.01	0.080 $\pm$ 0.004	(2.67 $\pm$ 0.30) $\times 10^{-5}$
Air 600 °C	0.20 $\pm$ 0.01	0.143 $\pm$ 0.007	(2.98 $\pm$ 0.50) $\times 10^{-5}$
no annealing	0.30 $\pm$ 0.01	0.021 $\pm$ 0.008	(1.90 $\pm$ 0.74) $\times 10^{-4}$
<i>Other particle sizes, no annealing</i>			
75–150 $\mu\text{m}$	0.07 $\pm$ 0.01	0.022 $\pm$ 0.007	(1.38 $\pm$ 0.28) $\times 10^{-4}$
300–600 $\mu\text{m}$	0.02 $\pm$ 0.01	0.021 $\pm$ 0.008	(1.02 $\pm$ 0.26) $\times 10^{-5}$
2–4 mm	0.01 $\pm$ 0.01	0.021 $\pm$ 0.004	(4.17 $\pm$ 1.13) $\times 10^{-5}$

<sup>a</sup>Initial surface area and Ce<sup>3+</sup> fraction, measured within minutes of removal of furnace. <sup>b</sup>Surface area and Ce<sup>3+</sup> fraction, measured 1 day after dissolution.

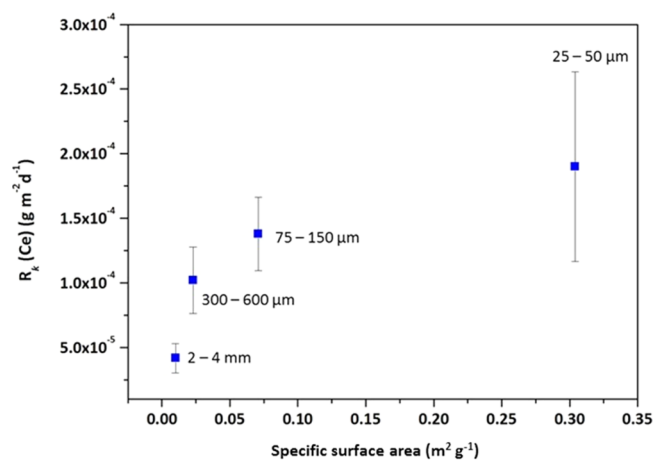


**Figure 6.** Normalized dissolution rates of Ce,  $R_k$  ( $\text{g m}^{-2} \text{ d}^{-1}$ ) as a function of specific surface area and particle size.

The surface area normalized dissolution rates were observed to increase with increasing surface area. This behavior is unexpected, since normalization to the surface area should result in similar dissolution rates. Samples of CeO<sub>2</sub> that were crushed and sieved to different size fractions clearly showed this correlation, with dissolution rates increasing from  $R_k = (4.17 \pm 1.13) \times 10^{-5} \text{ g m}^{-2} \text{ d}^{-1}$  for 2–4 mm particles to  $R_k = (1.38 \pm 0.28) \times 10^{-4} \text{ g m}^{-2} \text{ d}^{-1}$  for particles in the 75–150  $\mu\text{m}$  size fraction. The exposure of grain boundaries during particle crushing may be responsible for enhancing the reactive surface area, resulting in the observed trend, as follows: each particle is composed of a number of grains, with a grain size of 5–30  $\mu\text{m}$ . As the particle size decreases, from 2–4 mm to 75–150  $\mu\text{m}$ , the ratio of particle size to the number of grains also decreases. Because the grain size remains constant, the shrinking size of the particle exposes more grain boundaries to the dissolution medium. Grain boundaries are known to preferentially dissolve due to the presence of a greater number of energetically

reactive surface sites (e.g., defects) compared to the surfaces.<sup>11</sup> Once the smallest particle size is reached, each particle comprises only a few grains, with a high number of grain boundaries exposed to solution, which leads to the most rapid dissolution rates (Figure 6).

Similarly, thermally annealed particles of CeO<sub>2</sub> with the same particle size (25–50 μm) exhibited a factor of 7 decrease in their dissolution rate compared with nonannealed particles ( $R_k = (2.98 \pm 0.50) \times 10^{-5} \text{ g m}^{-2} \text{ d}^{-1}$  and  $(2.67 \pm 0.30) \times 10^{-5} \text{ g m}^{-2} \text{ d}^{-1}$ , for 600 and 1000 °C respectively), as shown in Figure 7. Because the reduction in surface area in these samples was

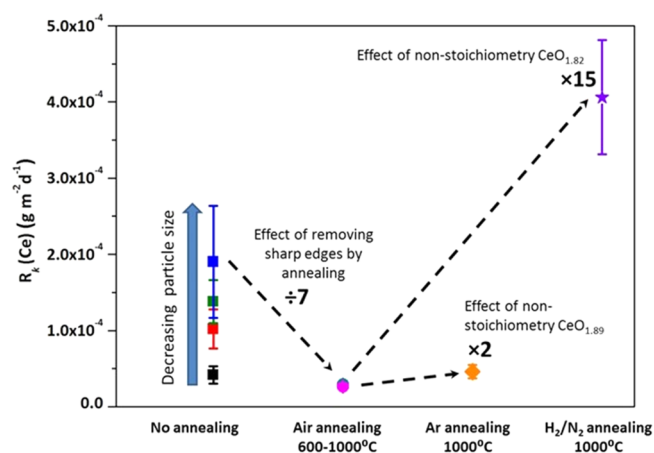


**Figure 7.** Summary of the normalized dissolution rates of Ce,  $R_k$  (g m<sup>-2</sup> d<sup>-1</sup>) as a function of particle size and annealing in air, Ar, and H<sub>2</sub>/N<sub>2</sub> atmospheres.

associated with the high temperature annealing of intrinsic defects and sharp edges generated through sample crushing, it can be concluded that these energetically reactive features influence the dissolution kinetics. This is in agreement with the

work of Claparede et al.<sup>13</sup> who found that increasing the sintering temperature of Th<sub>1-x</sub>Ce<sub>x</sub>O<sub>2</sub> powders led to a reduction in dissolution rate, attributed to the elimination of crystal defects and amorphous domains. The current work extends this hypothesis to samples prepared by crushing, generating surface defects in the form of “sharp edges”, as proposed by Corkhill et al.<sup>11</sup>

**3.4. Effect of Oxygen Vacancies on Dissolution Kinetics.** For CeO<sub>2</sub> samples annealed in different atmospheres at 1000 °C, the samples with the greatest oxygen vacancy content were found to dissolve at the most rapid rates. For example, the dissolution rate of CeO<sub>2</sub> annealed in Ar was slightly enhanced compared with CeO<sub>2</sub> annealed in air at the same temperature, by a factor of 2 (Table 3). The dissolution of CeO<sub>1.82</sub> (annealed in H<sub>2</sub>/N<sub>2</sub>) showed a significantly enhanced dissolution rate (Table 3, Figure 7). Samples of this material were analyzed by SEM at several time points during dissolution; in contrast to particles of stoichiometric CeO<sub>2</sub>, which did not change their shape or morphology upon 1 or 35 days of dissolution (Figure 8a–c), examination of the CeO<sub>1.82</sub> particles revealed a dramatic transformation. Prior to dissolution, these particles were 25–50 μm in size (Figure 6d), but within 1 day they were observed to break apart into smaller fragments ~5 μm in size, with a morphology suggestive of individual grains (Figure 8e). After 35 days of dissolution, some larger particles remained, but most of the sample had decomposed into single grain-sized fragments (Figure 8f). Post-dissolution BET analysis of these samples after 1 day of dissolution gave a surface area of  $2.49 \pm 0.01 \text{ m}^2 \text{ g}^{-1}$ , an increase by a factor of 5 compared with the initial surface area (Table 3). Normalization of the dissolution rate data to this surface area value gave a rate of  $R_k = (4.06 \pm 0.75) \times 10^{-4} \text{ g m}^{-2} \text{ d}^{-1}$ , 15 times greater than for air or Ar annealed samples of the same particle size (Figure 7). Due to the extremely rapid dissolution of this material, it was necessary to calculate the  $R_k$  between 0 and 1 day of dissolution, after which time the

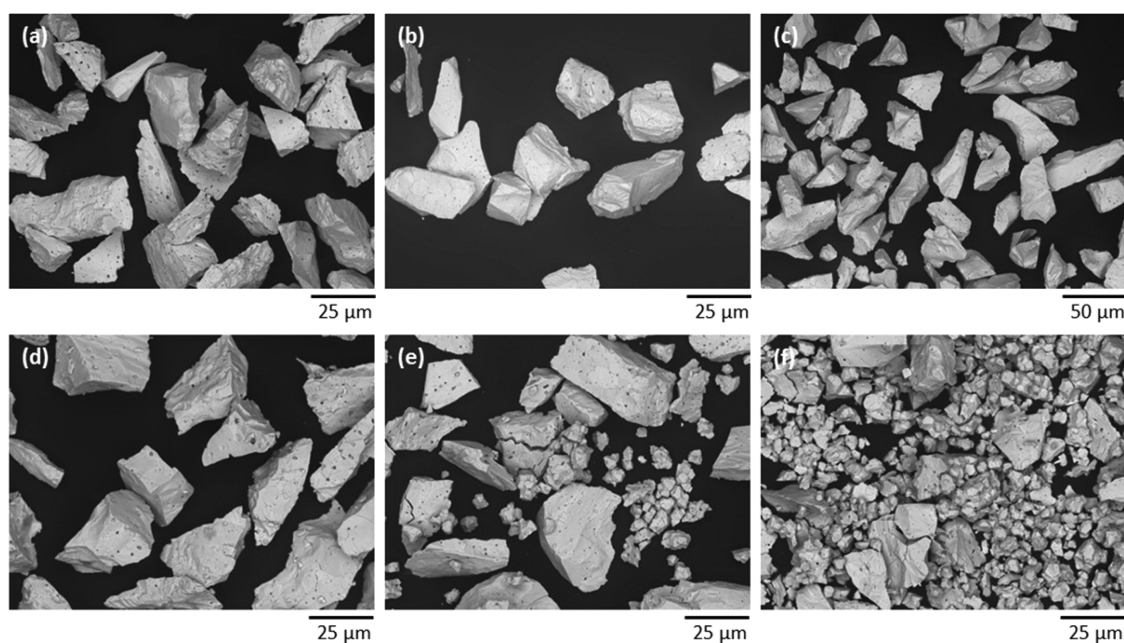


**Figure 8.** SEM images of 25–50 μm particles of non-annealed CeO<sub>2</sub> (a) prior to dissolution and after dissolution in 0.01 M HNO<sub>3</sub> at 90 °C for (b) 1 day and (c) 35 days; and H<sub>2</sub>/N<sub>2</sub> annealed CeO<sub>2-x</sub> (d) prior to dissolution; and after dissolution in 0.01 M HNO<sub>3</sub> at 90 °C for (e) 1 h and (f) 35 days.



normalized release of Ce was constant. When analyzed by XPS after 1 day of dissolution, these samples gave a surface stoichiometry of  $\text{CeO}_{1.96}$ , which indicates that a rapid oxidation of  $\text{CeO}_{2-x}$  occurred, concurrent with a significant reduction in the oxygen vacancy content.

## 4. DISCUSSION

**4.1. Microstructure and Surface Defect–Dissolution Rate Relationship in  $\text{CeO}_2$  and  $\text{CeO}_{2-x}$ .** A first-order expression that describes the concentration of Ce ( $C$ ) as a function of time ( $t$ ) has been considered

$$C = A(1 - e^{-bt}) \quad (4)$$

where  $A$  is the solubility limit of  $\text{CeO}_2$ , and  $b$  is the rate constant. Expanding eq 4 to account for the factors that are expected to contribute to the dissolution kinetics (surface area, oxygen vacancy content, and the different relative solubilities of  $\text{Ce}^{3+}$  and  $\text{Ce}^{4+}$ ) a first order dissolution rate expression can be derived for the  $\text{CeO}_2$  samples investigated in this study

$$C = \frac{S}{S_0}[\alpha A_3(1 - e^{-b_3 t}) + (1 - \alpha)A_4(1 - e^{-b_4 t})] \quad (5)$$

where  $S$  is the measured surface area (after dissolution in the case of  $\text{CeO}_{2-x}$ ),  $S_0$  is a reference surface area of  $1 \text{ m}^2 \text{ g}^{-1}$ ,  $\alpha$  is the fraction of  $\text{Ce}^{3+}$  (representing the oxygen vacancy content) at the particle surface as determined by XPS,  $A_3$  and  $A_4$  correspond to the solubility limits of  $\text{Ce}^{3+}$  and  $\text{Ce}^{4+}$  respectively, and  $b_3$  and  $b_4$  are the rate constants for  $\text{Ce}^{3+}$  and  $\text{Ce}^{4+}$ .

A genetic algorithm, which can be applied to solve constrained optimization problems,<sup>38</sup> was used to fit the individual parameters in eq 5, providing optimum solubility and rate constant values for  $\text{Ce}^{3+}$  and  $\text{Ce}^{4+}$  based on the dissolution data obtained in this study; the data and model fits are shown in Figure 9. The modeled  $\text{Ce}^{3+}$  and  $\text{Ce}^{4+}$  solubilities,  $A_3$  and  $A_4$ , gave best-fit values of  $(5.10 \pm 0.54) \times 10^{-4} \text{ mol dm}^{-3}$  and  $(1.59 \pm 0.08) \times 10^{-6} \text{ mol dm}^{-3}$ , respectively (errors represent the  $1\sigma$  confidence interval). These are in reasonable agreement with geochemically modeled solubility values, for example,  $\text{Ce}^{4+}$  solubility was calculated using PHREEQC (LLNL database) to be  $4.01 \times 10^{-6} \text{ mol dm}^{-3}$ . When considering only  $\text{CeO}_2$  annealed at various temperatures in air, and  $\text{CeO}_2$  particles of different sizes (shown in Figures 9a and b, respectively), the rate constant for  $\text{Ce}^{3+}$  was found to be  $b_3 = (0.245 \pm 0.06) \text{ d}^{-1}$ . For  $\text{Ce}^{4+}$  the scatter in the experimental data, combined with the low absolute solubility limit, resulted in poorly defined estimates for  $b_4$ ; a value of the order  $1.00 \times 10^{-7} \text{ d}^{-1}$  is tentatively suggested. Because the model to data fit was in agreement for  $\text{CeO}_2$  (Figure 9a and b), and the solubilities of the different Ce oxidation states were similar to geochemically modeled solubility values, it can be surmised that the parameters in eq 5 adequately describe the dissolution rate of stoichiometric  $\text{CeO}_2$ .

Figure 9c shows the dissolution data and model fit for  $\text{CeO}_{2-x}$  samples annealed in Ar and  $\text{H}_2/\text{N}_2$  atmospheres. The model fit to the parameters in eq 5 agrees somewhat with samples annealed in Ar; however, the model fit to the parameters is not in agreement with data from samples annealed in  $\text{H}_2/\text{N}_2$ , despite normalization to the post-dissolution surface area and consideration for the elevated content of the more highly soluble  $\text{Ce}^{3+}$  species in this sample (eq 5). Surface area data in Table 3 show that during dissolution, the surface area of  $\text{CeO}_{2-x}$

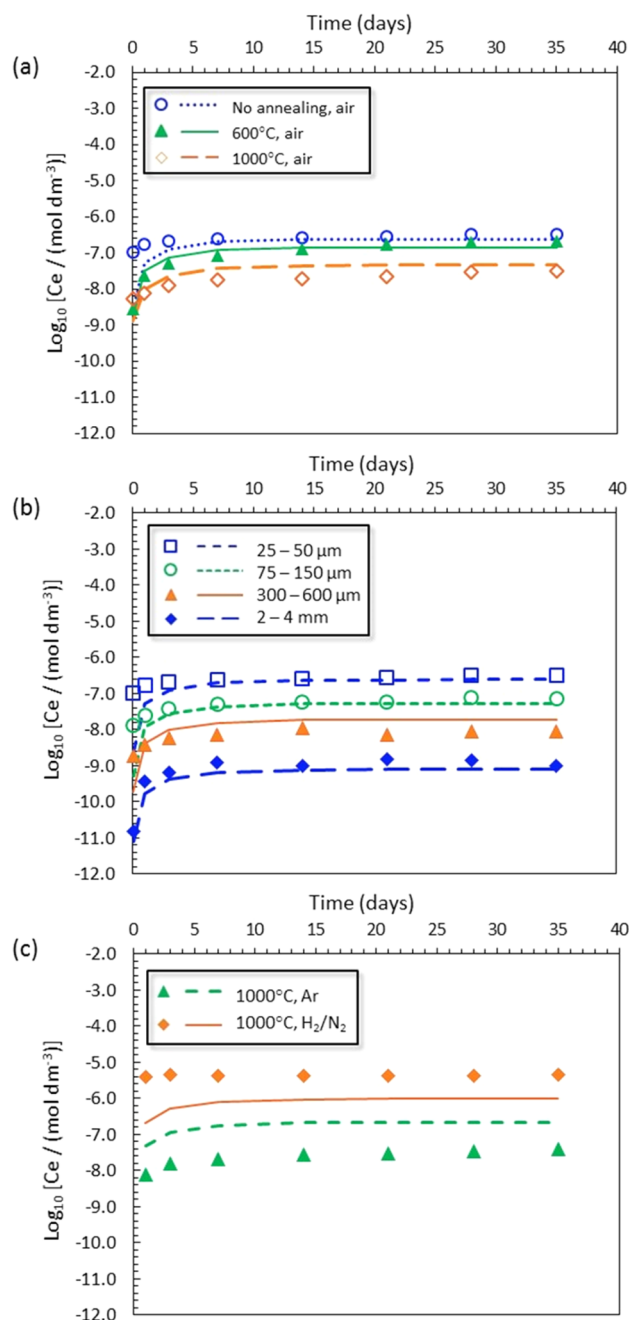


**Figure 9.** Ce concentrations ( $\text{mol dm}^{-3}$ ) derived from dissolution at  $90^\circ\text{C}$  in  $0.01 \text{ M HNO}_3$  (points) compared with modeled fit to eq 5 (lines) for (a)  $25\text{--}50 \mu\text{m}$   $\text{CeO}_2$  subject to different annealing temperatures in air; (b)  $\text{CeO}_2$  crushed to different size fractions, with no subsequent annealing; and (c)  $25\text{--}50 \mu\text{m}$   $\text{CeO}_2$  subject to annealing in different atmospheres at  $1000^\circ\text{C}$ . The parameters in eq 5 do not fit the data for  $\text{H}_2/\text{N}_2$  annealed samples shown in (c), suggesting another factor may contribute to the dissolution rate.

annealed in a  $\text{H}_2/\text{N}_2$  atmosphere increased by a factor of 5 after 1 day of dissolution. The first order dissolution model described above predicts that a surface area increase of a factor of 50 would be required to create a good fit to the parameters in eq 5, assuming all other values are correct. Specific surface area, as measured by BET, is routinely accepted to be the same as reactive surface area. However, recent studies have discussed that this may not necessarily be the case due to different activation energies of different high energy surface sites, e.g.,

grain boundaries and oxygen vacancies.<sup>39</sup> It is possible that the BET surface area measurements taken here, 1 day after dissolution, underestimated the reactive surface area of these samples during the initial stages of dissolution due to the presence of a high proportion of exposed grain boundaries, which are known to be significantly more reactive than the bulk.

**4.2. Physical Effects of Oxidation on the Kinetics of Dissolution.** As described above, not only the enhanced chemical solubility of  $\text{Ce}^{3+}$  influenced the dissolution kinetics of  $\text{CeO}_{2-x}$  but also the physical effects leading to a change in the sample surface area played a significant role. The mechanism through which this is postulated to occur for  $\text{CeO}_{2-x}$  investigated in the current study is described below.

Upon contact with air or an oxidic solution, the  $\text{Ce}^{3+}$  ions in  $\text{CeO}_{2-x}$  present as a result of charge compensation for oxygen vacancies, were rapidly oxidized to  $\text{Ce}^{4+}$ . Due to the difference in ionic radius between  $\text{Ce}^{3+}$  and  $\text{Ce}^{4+}$  (with  $\text{Ce}^{4+}$  the smaller cation), this oxidation process was associated with a contraction of the fluorite unit cell volume, on the order of  $\Delta V = -3.25 \pm 0.06 \text{ \AA}^3$  according to Rietveld analysis of XRD data (a  $6.0 \pm 0.1\%$  volume decrease relative to the starting volume). Ceramic materials that have undergone volume change-related phase transition exhibit significant internal lattice strain; according to Rietveld analysis, the lattice strain was initially high in  $\text{CeO}_{2-x}$  reducing by a factor of 2.6 during oxidation to  $\text{CeO}_2$ . Additionally, the presence of oxygen vacancies results in enhanced oxygen mobility, especially at grain boundaries where it is expected that a higher proportion of  $\text{Ce}^{3+}$  exists;<sup>35</sup> this facilitates preferential dissolution of grain boundaries.<sup>11</sup> In this study, during the dissolution of  $\text{CeO}_{1.82}$  to  $\text{CeO}_{1.96}$ , the combined influence of lattice strain and enhanced oxygen mobility, created by the removal of oxygen vacancies, resulted in the disintegration of particles, preferentially along grain boundaries, producing individual grain-sized fragments after 1 day of dissolution (Figure 8e–f). Importantly, this resulted in an increase in reactive surface area, which exposed fresh surfaces for dissolution and enhanced the overall dissolution rate. After 1 day, the dissolution rate was observed to be more or less constant, likely because there is reduced oxygen atom mobility within the nearly stoichiometric  $\text{CeO}_{1.96}$ . Hence, the combined roles of oxygen vacancies and grain boundaries should be considered significant in defining the dissolution kinetics of nonstoichiometric  $\text{CeO}_2$  and other fluorite-type materials.

The dual role of oxygen vacancies and grain boundaries in dissolution has been observed in other fluorite-type materials, albeit those comprising a solid solution of different chemical species. For example, Horlait et al.<sup>17</sup> reported the “crumbling” of  $\text{Ce}_{1-x}\text{Ln}_x\text{O}_{2-x/2}$  materials along grain boundaries during dissolution. This was associated with an increase in reactive surface area by up to a factor of 5. It was postulated that the incorporation of  $\text{Ln}^{3+}$  played a significant role in the dissolution mechanism through changes to the lattice volume.<sup>17,40</sup> Similarly, Finkeldei et al.<sup>41</sup> found that defect fluorite and pyrochlore structures in the  $\text{ZrO}_2\text{--Nd}_2\text{O}_3$  group preferentially dissolved along grain boundaries and at triple junctions, leading to disintegration. Substitution of elements into a fluorite lattice results in a volume change due to the difference in ionic radius of the substituting element;<sup>36</sup> the current study highlights the equally important role of oxygen vacancies on lattice volume change when only a single chemical species is present ( $\text{CeO}_2$ ), confirming the importance of this defect feature in dissolution rate kinetics.

The association of defect structures with grain boundaries and their influence on the dissolution of  $\text{CeO}_2$  and  $\text{ThO}_2$  analogues for spent fuel was recently hypothesized by Corkhill et al.,<sup>11</sup> who showed that the dissolution of grain boundaries was influenced by the crystallographic orientation of the grains and the corresponding mean misorientation angle of the grain boundaries. Boundaries with higher mean misorientation angles were found to dissolve at faster rates than those with low mean misorientation angles; it was hypothesized that higher misorientation angle grain boundaries contained a greater proportion of defects, with a high reactive surface area, which led to the enhanced dissolution rates. This study and others<sup>17,18</sup> have highlighted the important role of grain boundaries and particularly their association with defect structures (e.g., oxygen vacancies) on dissolution processes in spent fuel analogues. This underlines the requirement for new methodologies capable of linking grain boundary structure with dissolution kinetics, to fully understand their role in the dissolution of spent fuel materials.<sup>42</sup>

**4.3. Implications for the Dissolution of Spent Fuels.** It was recently demonstrated for a suite of fluorite type materials, including  $\text{CeO}_2$ ,  $\text{CaF}_2$ , and  $\text{UO}_2$ , that the surface stability is correlated with the proportion of high energy surfaces, even when different chemical processes of dissolution occur, for example for  $\text{CeO}_2$  and  $\text{CaF}_2$ .<sup>8</sup>  $\text{ThO}_2$  has also been shown to confirm this hypothesis.<sup>11,19</sup> Together with the results presented herein, these findings highlight the potential for energetically reactive surface sites to play a role in  $\text{UO}_2$  dissolution.

Spent  $\text{UO}_2$  fuel forms a complicated defect structure during fission within a reactor, and it is not yet clear the extent to which different types of reactive surface sites may influence the dissolution kinetics of spent fuel; however, studies on SIMFUEL have shown that doping with trivalent rare elements (to simulate fission products) resulted in lattice contraction<sup>12</sup> and a loss of cubic symmetry. On the basis of the results presented in the current study, we can hypothesize that such a lattice modification may lead to grain boundary decohesion. Evidence supporting this hypothesis includes a study of  $\text{UO}_2$  fuel stored in aerated, moist environments, which was found to degrade along its grain boundaries and become heavily fractured.<sup>43</sup> The effects of lattice volume change on the integrity of grain boundaries in these materials, and the extent to which it may affect the dissolution kinetics, requires further exploration. Recent work has shown that Mixed Oxide Fuels (MOx), containing  $\text{Pu}^{3+}$ , with a  $\text{PuO}_{2-x}$  stoichiometry of  $\text{PuO}_{1.61}$ ,<sup>44</sup> may also be prone to accommodating oxygen vacancies,<sup>45</sup> although the distribution of such defects between grains and the grain boundaries is currently not known. In light of the current limited knowledge of the atomic-scale structure of spent fuels, further work is required on inactive analogues,  $\text{UO}_2$ , and spent fuel materials to ascertain the effects of reactive surface sites on dissolution kinetics, as distinct from oxidative dissolution or radiolysis effects, to reduce the uncertainty associated with the prediction of spent fuel dissolution within a geological disposal facility.

## 5. CONCLUSIONS

We present an investigation of the role of energetically reactive surface sites on the initial dissolution rate of  $\text{CeO}_2$  to ascertain whether these features may result in overestimation of dissolution rates in the laboratory. Reactive surface sites and “sharp edges” were simulated by crushing samples to different



size fractions and through high temperature annealing. Oxygen vacancy defects in  $\text{CeO}_{2-x}$  were generated by high temperature annealing in oxygen-free conditions. Surface area was used as a measurement of “sharp edges” and intrinsic defects, and the total  $\text{Ce}^{3+}$  fraction measured by XPS was used as a measurement of the oxygen vacancy concentration. The relative dissolution rates of these materials showed that there was a quantifiable relationship between energetically reactive surface sites and dissolution rate, which was dependent upon reactive surface site concentration and the solubilities of  $\text{Ce}^{3+}$  and  $\text{Ce}^{4+}$ ; the greater the concentration of reactive surface sites, the higher the dissolution rate. The elimination of oxygen vacancies in  $\text{CeO}_{2-x}$  was found to significantly influence the dissolution rate; this was associated with changes in the lattice volume and lattice strain, manifested as grain boundary decohesion and increased surface area. Thus, it is clear that reactive surface sites, including artifacts of sample preparation, intrinsic material defects, and grain boundaries, have the potential to significantly enhance the dissolution of spent oxide fuel. We show that such effects can be quantified, thus it is possible to reduce the uncertainty associated with laboratory measurements of  $\text{UO}_2$  dissolution, albeit in a simplified analogue system. It will be essential to develop further careful studies designed to interrogate the effect of reactive surface features on the durability and dissolution of materials such as  $\text{UO}_2$  and  $\text{MO}_x$ , as distinct from solubility, surface area, and radiation effects.

## AUTHOR INFORMATION

### Corresponding Authors

\*Phone: 44 (0)1142223632. E-mail: [c.corkhill@sheffield.ac.uk](mailto:c.corkhill@sheffield.ac.uk).

\*Phone: 44 (0)1142225502. E-mail: [n.c.hyatt@sheffield.ac.uk](mailto:n.c.hyatt@sheffield.ac.uk).

### Notes

The authors declare no competing financial interest.

## ACKNOWLEDGMENTS

The research leading to these results has received funding from the European Atomic Energy Community's Seventh Framework Programme (FP7) under grant agreement No. 269903, The REDUPP (REDucing Uncertainty in Performance Prediction) project. We wish to give special thanks to the late Dr. Paul Wincott (University of Manchester) for assistance with XPS data collection. We are grateful to Dr. Virginia Oversby and Dr. Lena Z. Evins for invaluable discussion and support throughout the project. C.L.C. is grateful to The University of Sheffield for the award of a Vice Chancellor's Fellowship and EPSRC for the award of an ECR Fellowship (EP/N017374/1), N.C.H. acknowledges support from the Royal Academy of Engineering and the Nuclear Decommissioning Authority for funding, D.J.B. acknowledges financial support from the EPSRC Nuclear FiRST Doctoral Training Centre (EP/G037140/1), and F.Y.T. acknowledges support from the EPSRC PACIFIC programme (EP/L018616/1). We thank EPSRC and University of Sheffield Knowledge Transfer Account, under grant reference EP/H500170/1 for financial support. This research was performed, in part, at the MIDAS facility, at the University of Sheffield, which was established with support from the Department of Energy and Climate Change.

## REFERENCES

- (1) Cui, D.; Low, J.; Spahiu, K. Environmental Behaviours of Spent Nuclear Fuel and Canister Materials. *Energy Environ. Sci.* **2011**, *4*, 2537–2545.
- (2) Oversby, V. M. Uranium Dioxide, SIMFUEL and Spent Fuel Dissolution Rates – A Review Of Published Data. *SKB Technol. Rep.* **1999**, TR-99-22.
- (3) Shoesmith, D. W. Used Fuel and Uranium Dioxide Dissolution Studies – A Review. *Nucl. Waste Manage. Org. Rep.* **2007**, NMWO TR-2007-03.
- (4) Smellie, J.; Karlson, F. A Reappraisal of Some Cigar Lake Issues of Importance to Performance Assessment. *SKB Technol. Rep.* **1996**, TR 96-08.
- (5) Bruno, J.; Spahiu, K. The Long-Term Effect of Hydrogen on the  $\text{UO}_2$  Spent Fuel Stability under Anoxic Conditions: Findings from the Cigar Lake Natural Analogue Study. *Appl. Geochem.* **2014**, *49*, 178–183.
- (6) White, A. F.; Brantley, S. L. The Effect of Time in the Weathering of Silicate Minerals: Why do Weathering Rates Differ in the Laboratory and the Field? *Chem. Geol.* **2003**, *202*, 479–506.
- (7) Fischer, C.; Kurganskaya, I.; Schafer, T.; Luttge, A. Variability of Crystal Surface Reactivity: What do we Know? *Appl. Geochem.* **2014**, *43*, 132–157.
- (8) Maldonado, P.; Godinho, J. R. A.; Evins, L. Z.; Oppeneer, P. M. Ab Initio Prediction of Surface Stability of Fluorite Materials and Experimental Verification. *J. Phys. Chem. C* **2013**, *117*, 6639–6650.
- (9) Ollila, K.; Oversby, V. M. Dissolution of Unirradiated  $\text{UO}_2$  and  $\text{UO}_2$  Doped with  $^{233}\text{U}$  Under Reducing Conditions. *SKB Technol. Rep.* **2005**, TR-05-07.
- (10) Ollila, K. Dissolution of Unirradiated  $\text{UO}_2$  and  $\text{UO}_2$  Doped with  $^{233}\text{U}$  in 0.01M NaCl Under Anoxic and Reducing Conditions. *Posiva Oy Rep.* **2006**, 2006–08.
- (11) Corkhill, C. L.; Myllykylä, E.; Bailey, D. J.; Thorber, S. M.; Qi, J.; Maldonado, P.; Stennett, M. C.; Hamilton, A.; Hyatt, N. C. Contribution of Energetically Reactive Surface Features to the Dissolution of  $\text{CeO}_2$  and  $\text{ThO}_2$  Analogues for Spent Nuclear Fuel. *ACS Appl. Mater. Interfaces* **2014**, *6*, 12279–12289.
- (12) Razdan, M.; Shoesmith, D. W. Influence of Trivalent-Dopants on the Structural and Electrochemical Properties of Uranium Dioxide ( $\text{UO}_2$ ). *J. Electrochem. Soc.* **2014**, *161*, H105–H113.
- (13) Claparede, L.; Clavier, N.; Dacheux, N.; Mesbah, A.; Martinez, J.; Szenknect, S.; Moisy, P. Multiparametric Dissolution of Thorium-Cerium Dioxide Solutions. *Inorg. Chem.* **2011**, *50*, 11702–11714.
- (14) Claparede, L.; Clavier, N.; Dacheux, N.; Moisy, P.; Podor, R.; Ravau, J. Influence of Crystallisation State and Microstructure on the Chemical Durability of Cerium-Neodymium Mixed Oxides. *Inorg. Chem.* **2011**, *50*, 9059–9072.
- (15) Horlait, D.; Clavier, N.; Szenknect, S.; Dacheux, N.; Dubois, V. Dissolution of Cerium(IV)-Lanthanide(III) Oxides: Comparative Effect of Chemical Composition, Temperature, and Acidity. *Inorg. Chem.* **2012**, *51*, 3868–3878.
- (16) Horlait, D.; Tocino, F.; Clavier, N.; Dacheux, N.; Szenknect, S. Multiparametric Study of  $\text{Th}_{(1-x)}\text{Ln}_x\text{O}_{(2-x/2)}$  Mixed Oxides Dissolution in Nitric Acid Media. *J. Nucl. Mater.* **2012**, *429*, 237–244.
- (17) Horlait, D.; Claparede, L.; Tocino, F.; Clavier, N.; Ravau, J.; Szenknect, S.; Podor, R.; Dacheux, N. Environmental SEM Monitoring of  $\text{Ce}_{1-x}\text{Ln}_x\text{O}_{2-x/2}$  Mixed-Oxide Microstructural Evolution During Dissolution. *J. Mater. Chem. A* **2014**, *2*, 5193–5203.
- (18) Szenknect, S.; Mesbah, A.; Horlait, D.; Clavier, N.; Dourdain, S.; Ravau, J.; Dacheux, N. Kinetics of Structural and Microstructural Changes at the Solid/Solution Interface During Dissolution of Cerium(IV)-Neodymium(III) Oxides. *J. Phys. Chem. C* **2012**, *116*, 12027–12037.
- (19) Myllykylä, E.; Lavonen, T.; Stennett, M.; Corkhill, C.; Ollila, K.; Hyatt, N. Solution Composition and Particle Size Effects on the Dissolution and Solubility of a  $\text{ThO}_2$  Microstructural Analogue for  $\text{UO}_2$  Matrix of Nuclear Fuel. *Radiochim. Acta* **2015**, *103*, 565–576.
- (20) Stennett, M. C.; Corkhill, C. L.; Marshall, L. A.; Hyatt, N. C. Preparation, Characterisation and Dissolution of a  $\text{CeO}_2$  Analogue for  $\text{UO}_2$  Nuclear Fuel. *J. Nucl. Mater.* **2013**, *432*, 182–188.
- (21) ASTM. *Standard test methods for determining chemical durability of nuclear, hazardous and mixed waste glasses and multiphase ceramics:*

*The Product Consistency Test (PCT)*; ASTM C 1285-02; American Society for Testing and Materials: Philadelphia, 2008.

(22) Shirley, D. A. High Resolution X-Ray Photoemission Spectrum of Valence Bands of Gold. *Phys. Rev. B* **1972**, *5*, 4709–4714.

(23) Balzar, D. Voight-Function Model in Diffraction-Line Broadening Analysis. In *Microstructure Analysis from Diffraction*; Snyder, R. L., Bunge, H. J., Fiala, J., Eds.; Int. Union of Crystall.: 1999.

(24) Thomas, A.; Dacheux, N.; Le Coustumer, P.; Brandel, V.; Genet, M. Kinetic and Thermodynamic Study of the Thorium Phosphate-Diphosphate Dissolution. *J. Nucl. Mater.* **2000**, *281*, 91–105.

(25) Claparede, L.; Tocino, F.; Szenknect, S.; Mesbah, A.; Clavier, N.; Moisy, P.; Dacheux, N. Dissolution of  $\text{Th}_{1-x}\text{U}_x\text{O}_2$ : Effects of Chemical Composition and Microstructure. *J. Nucl. Mater.* **2015**, *457*, 304–316.

(26) Dacheux, N.; Le Dû, J.; Brandel, V.; Genet, M.; Decambox, P.; Moulin, C. Solubility Tests on Various Uranium (IV) Phosphates. *New J. Chem.* **1996**, *20*, 507–514.

(27) Stetsovych, V.; Pagliuca, F.; Dvorak, F.; Duchon, T.; Vorokhta, M.; Aulicka, M.; Lachnitt, J.; Schernich, S.; Matolinova, I.; Veltruska, K.; Skala, T.; Mazur, D.; Myslivecek, J.; Libuda, J.; Matlon, V. Epitaxial Cubic  $\text{Ce}_2\text{O}_3$  Films via Ce-CeO<sub>2</sub> Interfacial Reaction. *J. Phys. Chem. Lett.* **2013**, *4*, 866–871.

(28) Bevan, D. J. M. Ordered Intermediate Phases in the System  $\text{CeO}_2 - \text{Ce}_2\text{O}_3$ . *J. Inorg. Nucl. Chem.* **1955**, *1*, 49–59.

(29) Romeo, M.; Bak, K.; El Fallah, J.; Le Normand, F.; Hilaire, L. XPS Study of the Reduction of Cerium Dioxide. *Surf. Interface Anal.* **1993**, *20*, 508–512.

(30) Burroughs, P.; Hamnet, A.; Orchard, A. F.; Thornton, G. Satellite Structure In The X-Ray Photoelectron Spectra of some Binary and Mixed Oxides of Lanthanum and Cerium. *J. Chem. Soc., Dalton Trans.* **1976**, *17*, 1686–1698.

(31) Pfau, A.; Schierbaum, K. D. The Electronic Structure of Stoichiometric and Reduced  $\text{CeO}_2$  Surfaces: An XPS, UPS and HREELS Study. *Surf. Sci.* **1994**, *321*, 71–80.

(32) Mullins, D. R.; Overbury, S. H.; Huntley, D. R. Electron Spectroscopy of Single Crystal and Polycrystalline Cerium Oxide Surfaces. *Surf. Sci.* **1998**, *409*, 307–319.

(33) Mamontov, E.; Egami, T. Structural Defects in a Nano-Scale Powder of  $\text{CeO}_2$  Studied by Pulsed Neutron Diffraction. *J. Phys. Chem. Solids* **2000**, *61*, 1345–1356.

(34) Kümmerle, E. A.; Heger, G. The Structures of  $\text{C-Ce}_2\text{O}_{3+\delta}$ ,  $\text{Ce}_7\text{O}_{12}$ , and  $\text{Ce}_{11}\text{O}_{20}$ . *J. Solid State Chem.* **1999**, *147*, 485–500.

(35) Hojo, H.; Mizoguchi, T.; Ohta, H.; Findlay, S. D.; Shibata, N.; Yamamoto, T.; Ikuhara, Y. Atomic Structure of a  $\text{CeO}_2$  Grain Boundary: The Role of Oxygen Vacancies. *Nano Lett.* **2010**, *10*, 4668–4672.

(36) Reid, D. P.; Stennett, M. C.; Hyatt, N. C. The Fluorite Moderated Structures of the  $\text{Gd}_2(\text{Zr}_{2-x}\text{Ce}_x)\text{O}_7$  Solid Solution: An Analogue for Pu Disposition. *J. Solid State Chem.* **2012**, *191*, 2–9.

(37) Heisbourg, G.; Hubert, S.; Dacheux, N.; Purans, J. Kinetic and Thermodynamic Studies of the Dissolution of Thoria-Urania Solid Solutions. *J. Nucl. Mater.* **2004**, *335*, 5–13.

(38) Ojovan, M.; Travis, K. P.; Hand, R. J. Thermodynamic Parameters of Bonds in Glassy Materials from Viscosity-Temperature Relationships. *J. Phys.: Condens. Matter* **2007**, *19*, 415107–415122.

(39) Luttge, A.; Arvidson, R. S.; Fischer, C. A Stochastic Treatment of Crystal Dissolution Kinetics. *Elements* **2013**, *9*, 183–188.

(40) Horlait, D.; Claparede, L.; Clavier, N.; Szenknect, S.; Dacheux, N.; Ravaux, J.; Podor, R. Stability and Structural Evolution of  $\text{Ce(IV)}_{1-x}\text{Ln(III)}_x\text{O}_{2/2}$  Solid Solutions: A Coupled  $\mu$ -Raman/XRD Approach. *Inorg. Chem.* **2011**, *50*, 7150–7161.

(41) Finkeldei, S.; Brandt, F.; Rozov, A. A.; Bukaemskiy, S.; Neumeier, S.; Bosbach, D. Dissolution of  $\text{ZrO}_2$  Based Pyrochlores in the Acid pH Range: A Macroscopic and Electron Microscopy Study. *Appl. Geochem.* **2014**, *49*, 31–41.

(42) Fischer, C.; Finkeldei, S.; Brandt, F.; Bosbach, D.; Luttge, A. Direct Measurement of Surface Dissolution Rates in Potential Nuclear Waste Forms: The Example of Pyrochlore. *ACS Appl. Mater. Interfaces* **2015**, *7*, 17857–17865.

(43) Wronkewicz, D. J.; Buck, E. C.; Bates, J. K. Grain Boundary Corrosion and Alteration Phase Formation During the Oxidative Dissolution of  $\text{UO}_2$  Pellets. *Mater. Res. Soc. Symp. Proc.* **1997**, *468*, 519–526.

(44) Degueldre, C.; Pin, S.; Poonosamy, J.; Kulick, D. A. Redox state of plutonium in irradiated mixed oxide fuels. *J. Phys. Chem. Solids* **2014**, *75*, 358–365.

(45) Conradson, S. D.; Begg, B. D.; Clark, D. L.; den Auwer, C.; Ding, M.; Dorhout, P. K.; Espinosa-Faller, F. J.; Gordon, P. L.; Haire, R. G.; Hess, N. J.; Hess, R. F.; Keogh, D. W.; Morales, L. A.; Neu, M. P.; Paviet-Hartmann, P.; Runde, W.; Tait, C. D.; Veirs, D. K.; Vilella, P. M. Local and Nanoscale Structure and Speciation in the  $\text{PuO}_{2+x}\text{y}(\text{OH})_{2\text{y}}\cdot z\text{H}_2\text{O}$  System. *J. Am. Chem. Soc.* **2004**, *126*, 13443–13458.